Available online at www.sciencedirect.com
ScienceDirect
Journal of Sound and Vibration 305 (2007) 795–807
JOURNAL OF SOUND AND VIBRATION
www.elsevier.com/locate/jsvi

Numerical investigation of tire standing wave using 3-D patterned tire model

J.R. Cho[a,*], K.W. Kim[b], H.S. Jeong[b]

[a]*School of Mechanical Engineering, Pusan National University, Kumjung-Ku, Busan 609-735, Korea*
[b]*Kumho Tire Company Limited, Kwangju 506-711, Korea*

Received 3 November 2006; received in revised form 12 February 2007; accepted 29 April 2007
Available online 15 June 2007

Abstract

The tire standing wave is one of the crucial factors that may lead to unexpected tire structural failure because the total strain energy of the tire dramatically increases when it occurs. However, its analytical analysis has been limited owing not only to the complicated tire structure and material composition, but also to the problem nonlinearity. In this paper, its characteristics are numerically investigated with the help of the transient dynamic rolling analysis of the 3-D patterned tire model. The numerical reliability is assessed with the comparison of critical speeds with the experimental results and those obtained with the simple tire model. Also, the effects of the tire inflation pressure and the vertical load on the critical speed are parametrically investigated.

1. Introduction

When an inflated pneumatic tire rolls on the ground above some critical speed, it shows a wave-like deformation in the circumferential direction near and behind the tire contact region. This wavy deformation starts at the leading edge of the contact patch and spreads out to the region far behind the contact patch with the increase of the rolling speed [1]. This is known as the *standing wave* and it remains stationary, without rotating with tire. The occurrence of the standing wave accompanies the abrupt increase of the total strain energy, the heat generation rate and the rolling resistance of the tire, so that not only the fuel economy decreases considerably, but also the tire reaches structural failure within minutes. Owing to this detrimental feature, both the understanding of the standing wave mechanism and the prediction of its critical speed have been an important research subject in the tire mechanics community for several decades [2–4].

According to our literature survey, the phenomenon of the tire standing wave has been investigated mostly by experimental or analytical approaches. Even though the onset of the tire standing wave can be detected roughly by the naked eye [2,5], the accurate determination of its critical speed by experiment needs a modal analysis of tires utilizing a CCD camera/video system [4,6] or the Moiré fringe technique [7]. Needless to say, this experimental procedure is cost- and time-consuming, and becomes more crucial for high-frequency

*Corresponding author. Tel.: +82 51 510 2467; fax: +82 51 514 7640.
E-mail address: jrcho@pusan.ac.kr (J.R. Cho).

0022-460X/$ - see front matter © 2007 Elsevier Ltd. All rights reserved.
doi:10.1016/j.jsv.2007.04.049

standing waves. On the other hand, the analytical study, initiated by Turner [8] in 1951, derived the simplest critical speed estimate using a membrane strip reinforced with bias cords. After that, it evolved through subsequent investigators to ring-type models [2,9,10], toroidal membrane models [4,11] and thin shell models [12,13]. Using one of these models, the phenomenon of the standing wave is interpreted based on the wave propagation concept or natural frequencies and modes.

Even though the analytical study using such models helped one understand the fundamentals of the tire standing wave, its accuracy and applicability were not satisfactory because the complex material and structural composition of the tire and the inherent problem nonlinearity of the standing wave phenomenon could not be considered. In order to overcome the shortcomings of the experiments and the limitation of the analytical methods, a numerical approach utilizing the finite element method was introduced in the early 1990s [14–16]. However, owing to the painstaking mesh generation and the limitation of computer facilities, the numerical analyses were performed with rather simple tire models that simplify the tread geometry. As a result, such simplification leads to a limitation of an accurate critical speed prediction because the behavior of the tire standing wave is strongly influenced not only by the boundary condition, but also by the total mass and the stiffness of the tire [12,13].

As an extension of our previous work [17,18], this study intends to investigate the standing wave using 3-D patterned tire models in which the detailed tread blocks and the complex material composition are fully considered. In the current study, the critical speed is measured at the time when the lateral deformation produces a standing wave with a wavelength. The damping effect is taken into consideration in a mass-proportional manner with the damping coefficient that was justified from the comparison with the experiments [17]. The numerical accuracy is assessed from the comparison with the experimental results and those predicted with a simple tire model. The parametric effects of the inflation pressure and the vertical load on the critical speed are also investigated.

The organization of this paper is as follows. Following the introduction, the standing wave phenomenon in tires is briefly described in Section 2. The construction of the 3-D patterned tire model and the finite element approximation of the damped dynamic rolling problem are also presented in Section 3. The verification and parametric numerical results of the tire critical speed are given in Section 4, and the final conclusion is made in Section 5.

2. Tire standing wave

A radial pneumatic tire is made of several components of complex structural composition, as depicted in Fig. 1(a). The roles of each component are well described in a book by Clark [1]. Among which, tread contacts directly with the ground and consists of a number of rubber blocks and grooves, which are designed in a complex pattern for the sake of the tire running performances. However, it has been simplified in the traditional tire models owing to the above-mentioned difficulties in the meshing and computation. Since the overall stiffness and mass of a tire are definitely influenced by the pattern of tread blocks and grooves, the

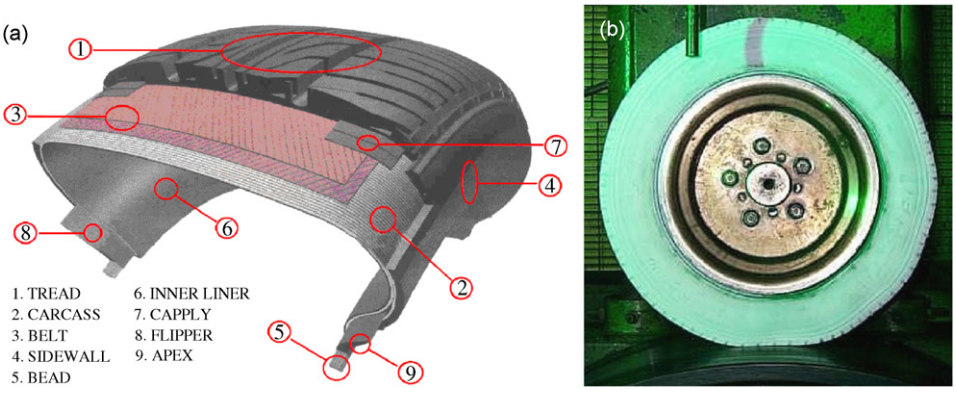

Fig. 1. A pneumatic tire: (a) structural composition and (b) standing wave experiment.

numerical accuracy of such simple tire models is highly questionable, particularly for the vibration analysis. Fortunately, thanks to the advances in modeling technologies and computer facilities, the patterned tire models in which detailed tread blocks and grooves are fully considered are [19,20] being introduced nowadays.

Fig. 1(b) depicts the experiment of the standing wave phenomenon, where a real tire installed on the rigid drum under the vertical load is forced to rotate up to the desired speed from a stationary position. A CCD camera-video system captures the tire shapes at various rotating speeds, and the captured digital images are examined frame by frame for the inspection of the standing wave [4,5]. Even though the frame rate of current video systems is limited for investigating steady standing wave patterns and furthermore the visual inspection cannot determine the critical speed accurately, the experiments that have been performed so far helped one understand qualitatively the essential features of the standing wave phenomenon.

Standing waves start to form near the leading edge of the contact region once the rolling speed reaches some critical value, and extend to the region far behind the trailing contact edge as the rotating speed increases further. Of course, this extension accompanies the increase of the amplitude and wavelength of standing waves and the temperature of the tire. Traditionally, standing waves had been thought to be caused by shocks, resonances, or instabilities of the tire [12,13], but Chatterjee et al. [4] reported that the formation of standing waves is not attributed to any of these. According to the analytical analysis of the nonlinear steady-state dynamic rolling of the balloon tire model, they found that the standing wave forms physically when the time scale of the tire rotation is shorter than one of the transient vibrations excited by the contact forces and the behavior of the standing wave is strongly influenced by the boundary conditions at the trailing contact edge.

Another eminent feature of the tire standing waves is the damped response due to the inherent viscoelastic properties of the underlying rubbers in the tire. The apparent evidence is the shifting of the standing wave behind the contact patch, the attenuation of its amplitude in the circumferential direction, the elongation of its apparent wavelength in proportional to the tire speed [5,12], and the bounding of the peak displacement at the critical speed. Furthermore, for small damping, standing waves start to form at a speed near the critical speed that is calculated by the resonance condition [13]. In this sense, the standing wave phenomenon in tires is also called a viscoelastic resonance response, but the resonance itself cannot be the physical origin of standing waves of the tire. This is because not only does the standing wave last for all higher rotation frequencies but also its size and shape change with the tire rolling speed [4].

Meanwhile, referring to a paper by Soedel [13], the critical rolling speed of tires is physically interpreted by the resonance condition

$$\Omega = \omega_n/n \tag{1}$$

in which Ω is the rotation speed of the contact force around the tire, n stands for the nth normal deflection mode of the tire in the circumferential direction (Fig. 2(a) represents the case of $n = 5$), and ω_n is the corresponding natural frequency of the tire. This condition was derived based upon the physical fact that the tire falls into resonance when the contact force travels from point A to point B (i.e. the wavelength λ of the nth normal deflection mode) at the same time as the period of oscillation $t = 2\pi/\omega_n$. Then, referring to Fig. 2(b),

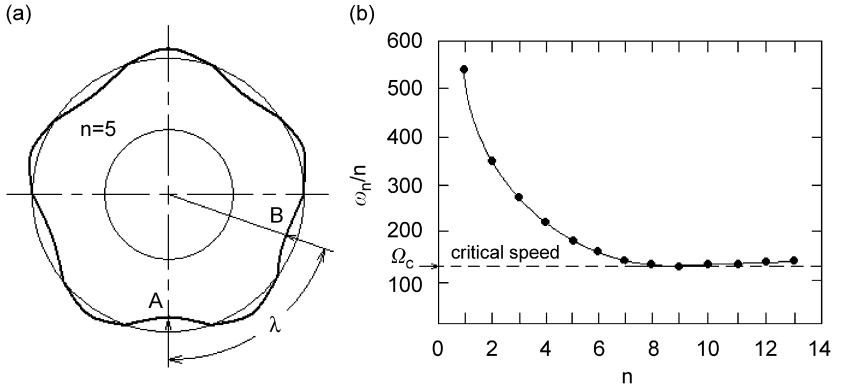

Fig. 2. Illustration: (a) the resonance condition and (b) the critical speed in undamped case.

the standing wave phenomenon appears first at the lowest rolling speed Ω_c given by

$$\Omega_c = (\omega_n/n)_{\min}. \tag{2}$$

It is worth noting that the onset of the standing wave in reality is at a speed higher than the theoretically determined value owing to the damping effect.

The underlying ideas of the traditional analytic methods for determining the critical speed, such as those using the wave propagation concept or natural frequencies and modes, can be interpreted by this resonance condition. For example, Chatterjee et al. [4] applied the above resonance condition to a toroidal membrane model and obtained the critical rolling speed given by

$$\Omega_c = \min_{n=1,2,\ldots} (\omega_n/n) = \sqrt{K}, \quad K = \bar{K}/\bar{k} \tag{3}$$

in which the undamped natural frequencies $\omega_n = \sqrt{1+n^2K}$ were analytically derived from the nonlinear boundary value problem associated with the steady-state rolling conditions, and $\bar{K}$ and $\bar{k}$ denote the radial (purely radial) stiffness and the shear (relative radial) stiffness of the toroidal membrane, respectively.

One can intuitively recognize from Eqs. (2) and (3) that the critical speed depends on the tire structure, the materials of the tire components, and the contact condition. As a result, the prediction reliability of critical speeds is definitely influenced by how accurately these factors are integrated into the analytical or numerical tire models.

3. Frictional dynamic rolling analysis of the patterned tire

3.1. 3-D patterned tire model

The material composition of most tires is distinguished largely by the fiber-reinforced rubber (FRR) parts and the remaining pure rubber part, as represented in Fig. 3(a). The FRR parts of the tire model considered here are composed of a single-ply polyester carcass, two steel belt layers, and several steel bead cords. Since the FRR parts are in the highly complex structure, their material models are chosen based upon the goal of the numerical simulation. In the static tire analysis, those parts are usually modeled using solid elements like rebar elements, and which do not cause too much trouble in the aspect of CPU time. But, in the dynamic tire analysis this full modeling requires an extremely long CPU time, so the FRR parts are modeled as either a composite membrane or a composite shell. In the current study, two belt layers in the underlying rubber matrix and a carcass layer shield with an inner-liner are modeled using composite shells. On the other hand, steel cords and the underlying rubber matrix in the bead region are modeled as a homogenized solid by utilizing the modified rule of mixtures [21]. Fig. 3(b) illustrates the modeling of the two belt layers in the underlying rubber matrix as a single layer composed of orthotropic shells in which individual steel wires and

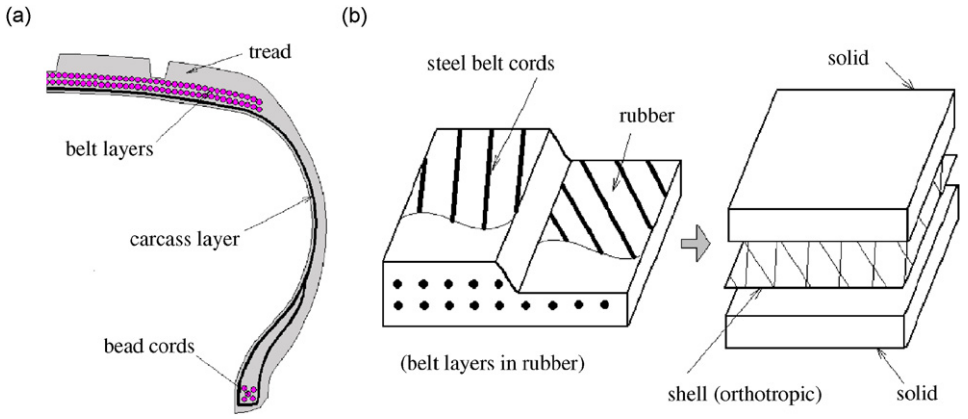

Fig. 3. Material modeling of tire: (a) material composition and (b) modeling of the belt layers.

rubber are treated as an isotropic and the equivalent composite material constants are calculated by the Halpin-Tsai formulation [22]. Note that shell and solid elements are coupled by the shell-to-solid constraint that is supported in ABAQUS [23].

Rubbers, except for the FRR parts, are modeled by the penalized first-order Moonley–Rivlin model in which the strain density function is defined by

$$W(J_1, J_2, J_3; K) = C_{10}(J_1 - 3) + C_{01}(J_2 - 3) + \frac{1}{K}(J_3 - 1)^2, \tag{4}$$

where J_i are the invariants of the Green–Lagrangian strain tensor, and C_{10} and C_{01} are the rubber material constants determined from the experiment. On the other hand, K is a sort of penalty parameter controlling the rubber incompressibility. The shear modulus τ and the bulk modulus κ of rubber are related as $2(C_{10} + C_{01}) = \tau$ and $K = 2\kappa$, from which one can easily obtain the following relation for Poisson's relation: $v = [3K/4(C_{10} + C_{01}) - 2]/[3K/2(C_{10} + C_{01}) + 2]$. It is clear that the incompressibility of rubber is asymptotically enforced as the penalty parameter approaches infinity, but the choice of K near 100 is usually recommended for the stable transient dynamic response with a reasonable time step size.

Fig. 4(a) shows a 2-D section mesh that is constructed according to the above-mentioned material modeling such that pure rubber solid, composite shell and homogenized solid elements are mixed, while Fig. 4(b) represents the corresponding 3-D patterned tire mesh that is generated by our in-house program [20]. The detailed tread mesh can be inserted either completely or partially, depending on the purpose of the tire analysis. For the static tire contact analysis to compute a footprint and contact pressure, the partial patterned tire model is recommended in respect to the CPU time. On the other hand, the dynamic contact analysis for the rolling resistance and hydroplaning requires the full patterned model.

Referring to our previous paper [20] in which the details on the tread mesh generation and the incompatible tying algorithm are addressed, the tread and body meshes with different mesh densities are separately generated at the beginning and then both are assembled by the incompatible surface-to-surface tying algorithm supported by AQAQUS [23]. The 3-D body mesh can be easily generated by a simple revolution of its 2-D section mesh, but the generation of the 3-D tread mesh is not so simple owing to the complexity of tread blocks and grooves. Thus, a 3-D tread mesh is constructed by utilizing a series of basic meshing operations.

3.2. Damped transient dynamic rolling analysis

The damped frictional dynamic rolling problem is formulated by the total Lagrangian method that refers to the original tire domain Ω^0, together with the penalty method to enforce the dynamic contact and the material incompressibility. Introducing iso-parametric finite element basis functions $\{\phi_I(\mathbf{X})\}_{I=1}^{N}$ into the penalized

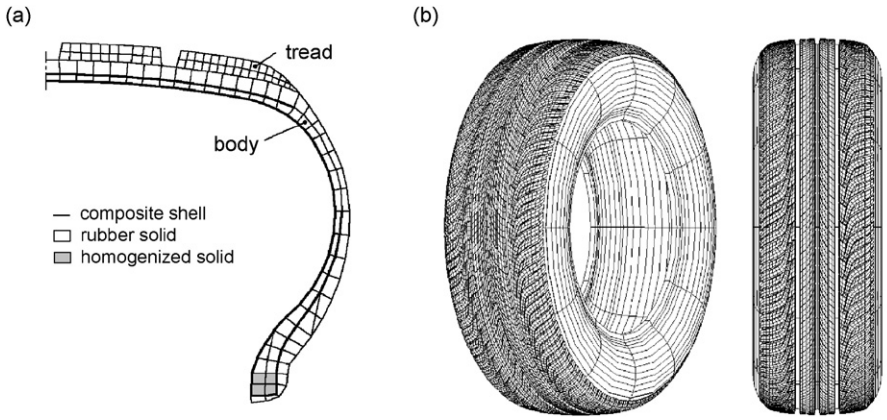

Fig. 4. Tire FEM meshes: (a) 2-D section mesh and (b) 3-D patterned mesh.

total Lagrangian formulation leads to the following matrix equations:

$$\mathbf{M}\ddot{\bar{\mathbf{u}}} + \mathbf{C}\dot{\bar{\mathbf{u}}} + \mathbf{F}_{\text{int}} = \mathbf{F}_{\text{ext}}, \tag{5}$$

with the nodal displacement vector $\bar{\mathbf{u}}$. By applying the mass-proportional damping model [24] only to the tire part Ω_R showing the significant lateral deformation, we have

$$\mathbf{C} = c\mathbf{I}_R\mathbf{M}, \tag{6}$$

with the damping coefficient c and the identity matrix $\mathbf{I}_R$ restricted to the partial tire region Ω_R. The mass matrix and two load vectors in Eq. (5) are defined by

$$\mathbf{M} = \int_{\Omega^0} \rho^0 \Phi^{\mathrm{T}} \Phi \, \mathrm{d}\Omega^0, \tag{7}$$

$$\mathbf{F}_{\text{int}} = \int_{\Omega^0} \mathbf{B}_0^{\mathrm{T}} \{\mathbf{S}(\mathbf{u})\} \, \mathrm{d}\Omega^0 + \int_{\partial\Omega_c^0} \mathrm{k_p} (\mathbf{n}\Phi)^{\mathrm{T}} \mathbf{n}\Phi \, \mathrm{ds}^0, \tag{8}$$

$$\mathbf{F}_{\text{ext}} = \int_{\Omega^0} \rho^0 \Phi^{\mathrm{T}} \mathbf{f} \, \mathrm{d}\Omega^0 + \int_{\partial\Omega_N^0} \Phi^{\mathrm{T}} \hat{\mathbf{t}}^0 \, \mathrm{d}s^0 + \int_{\partial\Omega_c^0} \left[\Phi^{\mathrm{T}} \mathbf{t}_T^0 + k_p g(\mathbf{n}\Phi)^{\mathrm{T}}\right] \mathrm{d}s^0, \tag{9}$$

where Φ is the $(3 \times 3N)$ matrix consisting of N basis functions and $\mathbf{n}$ is the inward unit vector normal to the contact boundary of the rigid road. On the other hand, $\mathbf{B}_0$ and $\{\mathbf{S}\}$ are the $(6 \times 3N)$ matrix and the (6×1) vector defined, respectively, as

$$\mathbf{B}_0 = \left\{\mathbf{B}_0^1, \ldots, \mathbf{B}_0^I, \ldots, \mathbf{B}_0^N\right\}, \tag{10}$$

$$\{\mathbf{S}\} = \left\{S_{xx}, S_{yy}, S_{zz}, S_{xy}, S_{yz}, S_{zx}\right\}^{\mathrm{T}}, \tag{11}$$

where $\mathbf{B}_0^I$ is the (6×3) matrix containing the terms $\partial\phi_I/\partial X_i$ multiplied by F_{jk} [25].

The observation time interval t^* is divided into a finite number of subintervals $t^n (n = 0, 1, 2, 3, \ldots)$, such that $t^{n+1} = t^n + \Delta t^n$. The lumped mass matrix $\tilde{\mathbf{M}}$ allows the equation of motion (5) to be written as

$$\ddot{\bar{\mathbf{u}}}^n = \tilde{\mathbf{M}}^{-1}\left(\mathbf{F}_{\text{ext}}^n - \mathbf{F}_{\text{int}}^n\right) - c\,\mathbf{I}_R\dot{\bar{\mathbf{u}}}^n \tag{12}$$

in the explicit time incremental form. We note that $\mathbf{F}_{\text{int}}^n$ and $\mathbf{F}_{\text{ext}}^n$ are defined by replacing $\mathbf{B}_0, \{\mathbf{S}\}, \mathbf{n}, \hat{\mathbf{t}}^0$ and $\mathbf{t}_T^0$ in Eqs. (8) and (9) with the values calculated at time stage t^n. According to the central difference method, time-step-wise velocities and displacements are determined through

$$\dot{\bar{\mathbf{u}}}^{n+\beta} = \dot{\bar{\mathbf{u}}}^{n-\beta} + \left(\Delta t^{n-1} + \Delta t^n\right) \ddot{\bar{\mathbf{u}}}^n/2, \tag{13}$$

$$\bar{\mathbf{u}}^{n+1} = \bar{\mathbf{u}}^n + \Delta t^n \, \dot{\bar{\mathbf{u}}}^{n+\beta}, \tag{14}$$

with β of 1/2. For the numerical convergence and stability, the time step size should satisfy the following condition:

$$\Delta t \le \frac{2}{\omega_{\max}}\left(\sqrt{1+\zeta^2} - \zeta\right) \tag{15}$$

determined with the largest element frequency $\omega_{\max}$ in the mesh and the critical damping ratio ζ corresponding to $\omega_{\max}$.

4. Numerical experiments

An automobile tire P205/60R15 with an unsymmetrical tread pattern is used for the standing wave simulation. Its patterned and simple FEM models are represented, respectively, in Figs. 5(a) and (b), where the rotating rigid drum has a radius equal to 1.7 m. In both FEM models, the FRR parts and the steel bead cords in the underlying rubber matrix are modeled with bilinear composite shell elements and tri-linear homogenized solid elements, respectively, while the remaining rubber parts are generated with tri-linear solid elements. The

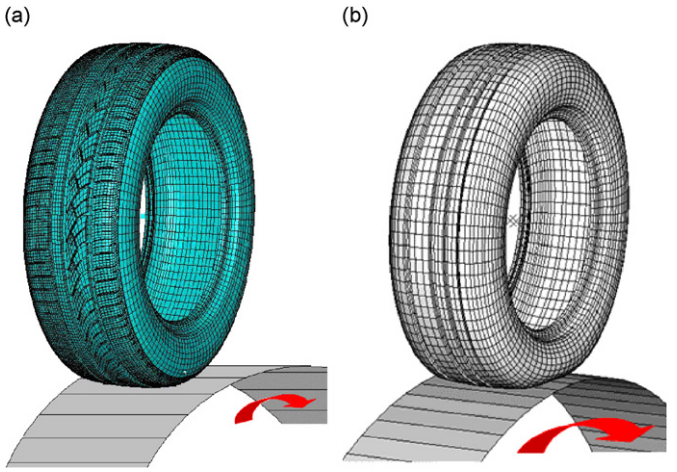

Fig. 5. Tire models for the standing wave simulation: (a) patterned and (b) simple.

Table 1
Structural composition and material properties of four different components of types A and B

Type	Item	Components			
		Carcass	Belt	Capply	Flipper
A	Number	2	2	2	1
	Angle (°)	+88/−88	+24/−24	0/0	+25
	EPI	24	20	30	22
	Modulus (GPa)	4.220	110.527	1.460	1.578
B	Number	1	2	2	0
	Angle (°)	+90	+21/−21	0/0	–
	EPI	30	18	30	–
	Modulus (GPa)	2.715	110.527	1.586	–

total node numbers of each tire mesh are as follows: 61,590 for the patterned tire mesh (32,754 of solid elements and 9360 of shell elements) and 22,680 for the simple tire mesh (17,820 of solid elements and 9180 of shell elements).

On the other hand, the rigid drum is modeled with rigid elements. The tire wheel is modeled with a number of massless rigid elements connecting the tire axis with all the outer nodes of the tire bead elements that are in contact with the tire rim. However, these rigid elements are excluded from both FEM meshes for the sake of clear representation. Meanwhile, the dynamic effect of the tire wheel is taken consideration by adding its total mass and moment of inertia to the tire axis. The standing wave simulation was carried out with the 4-cored SGI Altix 4700 supercomputer (each core has 2 CPUs of 1.6 GHz).

The critical speed is strongly influenced by the overall tire stiffness and the cord angle [2,8], so we consider two different types of P205/60R15 tire model in which only four components that are composed of cords have different structures and material properties, as given in Table 1, for the verification of the current study. The material and construction parameters of type B correspond to those of usual standard tires, while type A was selected to examine the critical speed of the durability-reinforced tires in which the stiffness of carcass and flipper is strengthened. Referring to Fig. 1(a), the inclination angles of cords in carcasses, belts, capplys and flipper are measured with respect to the circumferential direction of the tire, while EPI (ends per inch) stands for the number of cords within an inch in the direction normal to the cord axis. Detailed material properties of the remaining components, except for the four components, are referred to in our previous paper [26].

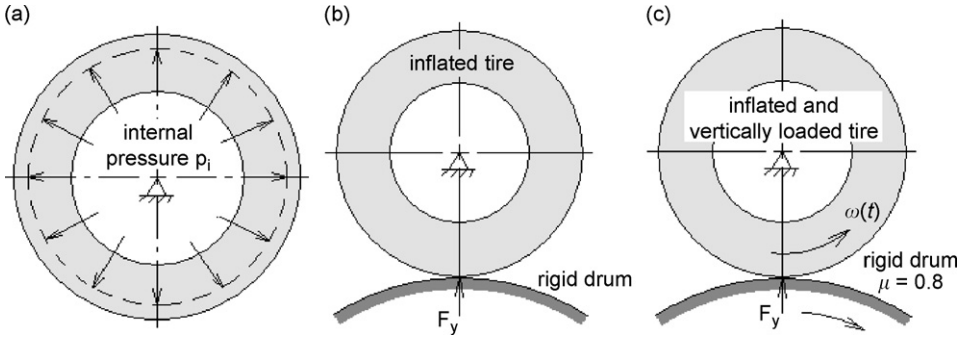

Fig. 6. Three sequential steps for the standing wave simulation: (a) inflation, (b) vertical contact, and (c) transient dynamic rolling.

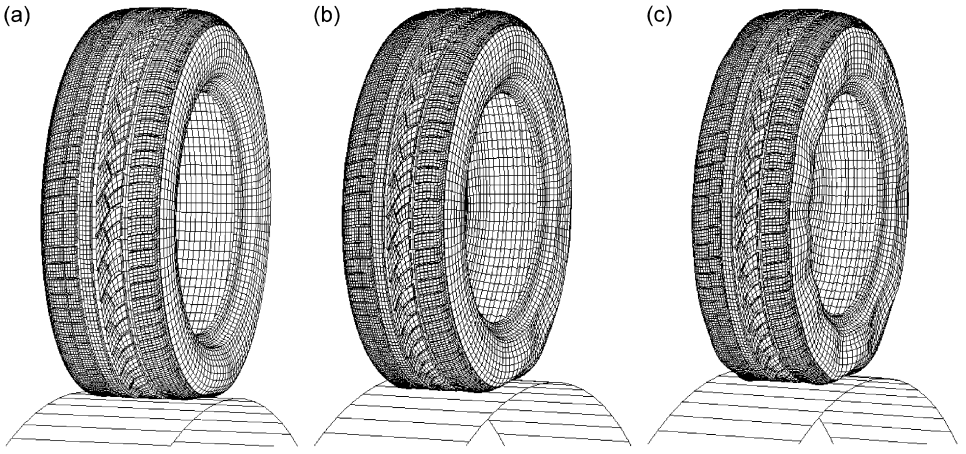

Fig. 7. Deformed configurations of the patterned tire model (type A): (a) 160 km/h, (b) 182 km/h, and (c) 220 km/h.

Referring to Fig. 6, a standing wave simulation of the patterned tire is carried out through three sequential steps. First, the tire is inflated up to the preset internal pressure p_i with the tire axis fixed. Then the bottom rigid drum is moved toward the tire by the vertical force F_y. Finally, the drum is forced to rotate clock-wise from a resting position, such that the angular velocity $\omega(t)$ of the tire increases linearly with the lapse of time. The frictional coefficient μ between the drum surface and the tire tread is set by 0.8. It was determined experimentally from the real standing wave test apparatus shown in Fig. 1(b). On the other hand, the relative bulk modulus κ/τ introduced to enforce the material incompressibility of the rubber and the penalty parameter k_p in Eqs. (8) and (9) are set, respectively, by 100 and 10 MPa, while the damping factor c is chosen by 0.49N s/m and the mass-proportional damping is applied to the inner-liner and sidewall elements that show a significant lateral deformation. The damping factor was chosen through the our previous work on the transient dynamic rolling analysis [17], where its value was tuned so as to the numerical simulation produces the dynamic responses close to the experimental results. We note that the last four parameters are set commonly throughout the numerical experiments in this paper.

4.1. Verification

Two types of P205/60R15 tires that are specified in Table 1 were tested numerically and experimentally with the same conditions: the inflation pressure $p_i = 137.9$ kPa (20 psi), the vertical load $F_y = 475$ kgf and the frictional coefficient $\mu = 0.8$. In order to cause the standing wave phenomenon at lower speeds, the inflation pressure was set lower than the normal pressure 206.85 kPa (30 psi) that is specified for P205/60R15 tire models, and which is usually adopted by most tire makers. The critical speed was measured at the time when the lateral deformation reaches the standing wave with a wavelength. Figs. 7(a) and 8(a) show the deformed

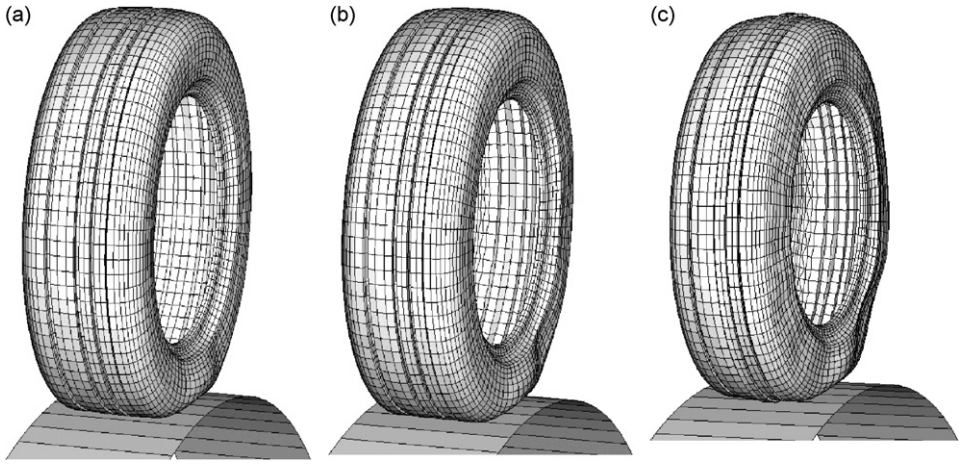

Fig. 8. Deformed configurations of the simple model (type A): (a) 160 km/h, (b) 205 km/h, and (c) 245 km/h.

Table 2
Comparison of the critical speeds (inflation pressure: 137.9 kPa, vertical load: 475 kgf)

Type	Critical speed V_c (km/h)		
	Numerical analysis		Experiment
	Patterned model	Simple model	
A	182 (4.21%)	205 (7.89%)	190
B	168 (2.32%)	190 (10.47%)	172

configurations of both tire models at the speed before the wavy deformation forms. On the other hand, Figs. 7(b) and 8(b) show the standing waves with only a wavelength in both tire models at each critical speed. The deformed configurations of both tire models when standing waves are completely formed in the circumferential direction are represented, respectively, in Figs. 7(c) and 8(c).

In Table 2, the critical speeds predicted by the finite element analyses are compared with those measured by an independent experiment, where the percentage values in parenthesis indicate the relative errors estimated with respect to the experimental results. Above all, one can figure out that the prediction accuracy of the patterned tire model is higher than the simple tire model, such that the maximum relative error is reduced by more than 50%. One interesting observation is that the critical speeds predicted by the simple tire model are vastly overestimated, which implies that the disregard of the detailed tread grooves results in a relative shear stiffness $\bar{K}$ in Eq. (3) higher than the actual value of the real patterned tire. The overestimation of the critical speed when the tread grooves and blocks are ignored has been also presented in the papers by Togo [2] and Brockman et al. [14]. Thus, it has been justified that the detailed tread geometry should not be ignored to get a reliable prediction of the tire critical speed. In this specific regard, the numerical accuracy of the patterned tire model can be additionally justified by our previous work [17] in which the resonance frequencies predicted by the patterned tire model are compared with the experimental results. The reason is because the critical speed is directly related to the resonance phenomenon, as mentioned earlier. Another noticeable thing is that type A produces a higher critical speed than type B in all three prediction methods, which is because the stiffness of carcass and flipper in type A is strengthened when compared to type B.

4.2. Parametric investigation

We performed the parametric experiments with the patterned tire model of type A to investigate the effects of the inflation pressure and the vertical load on the critical speed. The other simulation parameters, except for

Table 3
Variation of the critical speed to the inflation pressure and vertical load

Vertical load F_y (475 kgf)		Inflation pressure p_i (206.85 kPa)	
Pressure (kPa)	Critical speed (km/h)	Load (kgf)	Critical speed (km/h)
179.27 (85%)	193	404 (85%)	205
206.85 (100%)	199	475 (100%)	199
234.43 (115%)	203	546 (115%)	191

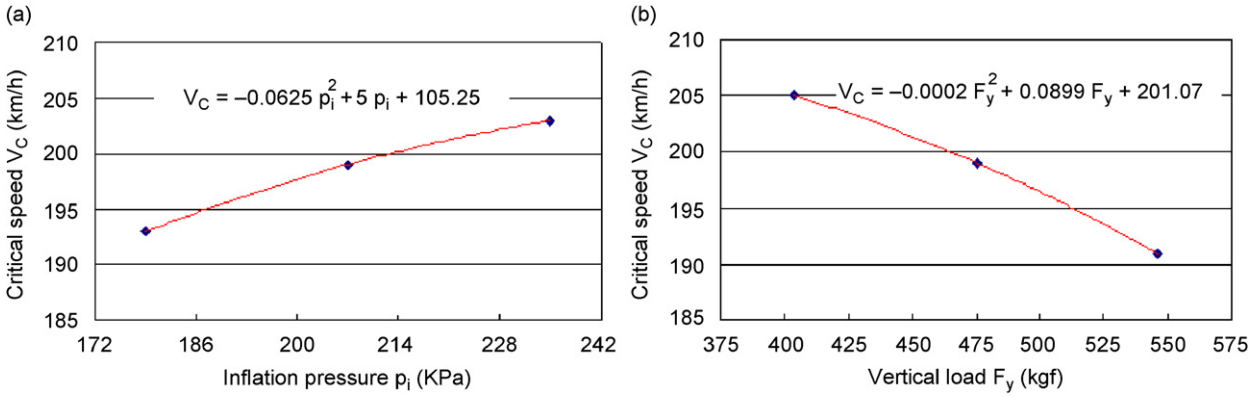

Fig. 9. Variation of the critical speed: (a) to the inflation pressure and (b) to the vertical load.

these two, were set as the same as the previous verification experiments. Three simulation cases were chosen for each parameter: normal, 15% below and 15% above. Referring to Table 3 and Fig. 9, the critical speed becomes higher as the inflation pressure increases, which is owing to the fact that a pneumatic tire becomes stiffer in proportion to the cord tension. This tendency agrees with the theoretical and experimental results by other investigators [2,4]. Thus, driving with tires inflated below a regulation pressure is done with a high danger of tire structural failure stemming from the standing wave phenomenon. On the other hand, the critical speed becomes lower as the vertical contact force increases. Referring to Figs. 1(b) and 2(a), together with a paper by Soedel [13], the standing wave deformation becomes a lower normal deflection mode as the vertical load increases because the contact zone of the tire becomes larger in proportional to the vertical load. Accordingly, the wavelength λ and the resulting time required for the vertical load to travel through a wavelength become longer, so that the critical speed goes down according to the resonance condition given in Eq. (1).

Time-histories of the total strain energy of the patterned tire model (type A) for different inflation pressures and vertical loads are represented respectively in Figs. 10(a) and (b), for which the vertical load for the former and the inflation pressure for the latter were set as 206.85 kPa and 475 kgf. All transient dynamic rolling simulations were completed within 1.5 s, including 0.35 s taken for the inflation and the static contact steps. Since the rigid drum was sped up along the time-angular velocity specification chart, the tire velocity at a specific time can be explicitly known. The total strain energies in both cases are observed to increase abruptly at critical speeds. Also, one can discover that the critical times showing the abrupt increase in the total strain energy are different for different pressures and loads, but those vary in the manner consistent with the parametric variation of critical speed.

Meanwhile, Figs. 11(a) and (b) represent time-histories of the total kinetic energy of the model tire, where all curves show a remarkable drop at critical speeds. Furthermore, the critical speeds for different pressures and loads show parametric variations that are consistent with those of the critical speed and the total strain energy.

Since the critical speed is significantly influenced not only by the inflation pressure but also by the vertical load, the investigation of the simultaneous effects of these parameters on the critical speed is of importance. Nine parametric cases were simulated and the numerical results are recorded in Table 4, where the critical

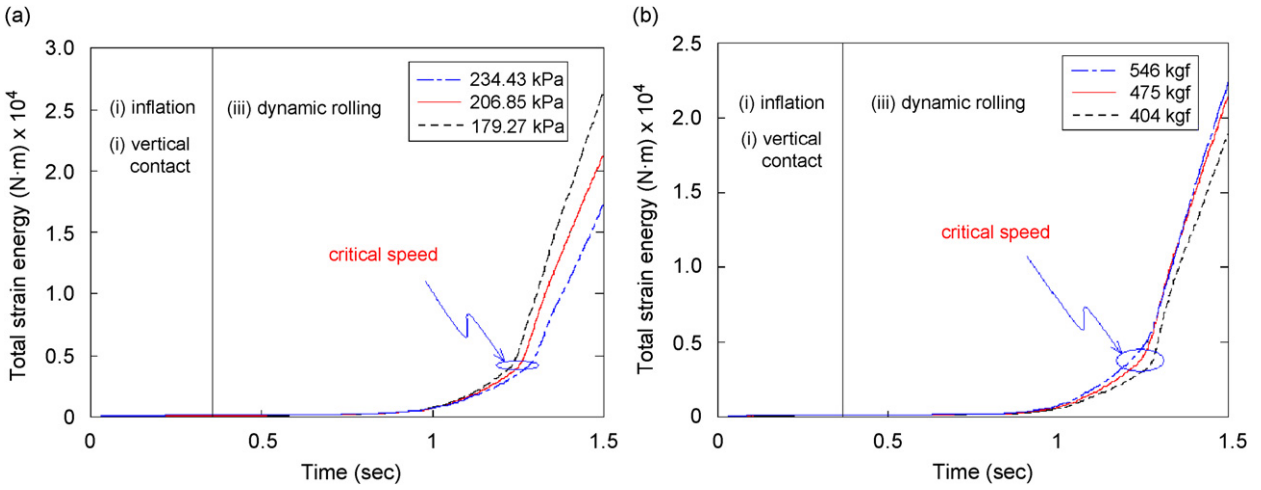

Fig. 10. Variation of the total strain energy: (a) to the inflation pressure and (b) to the vertical load.

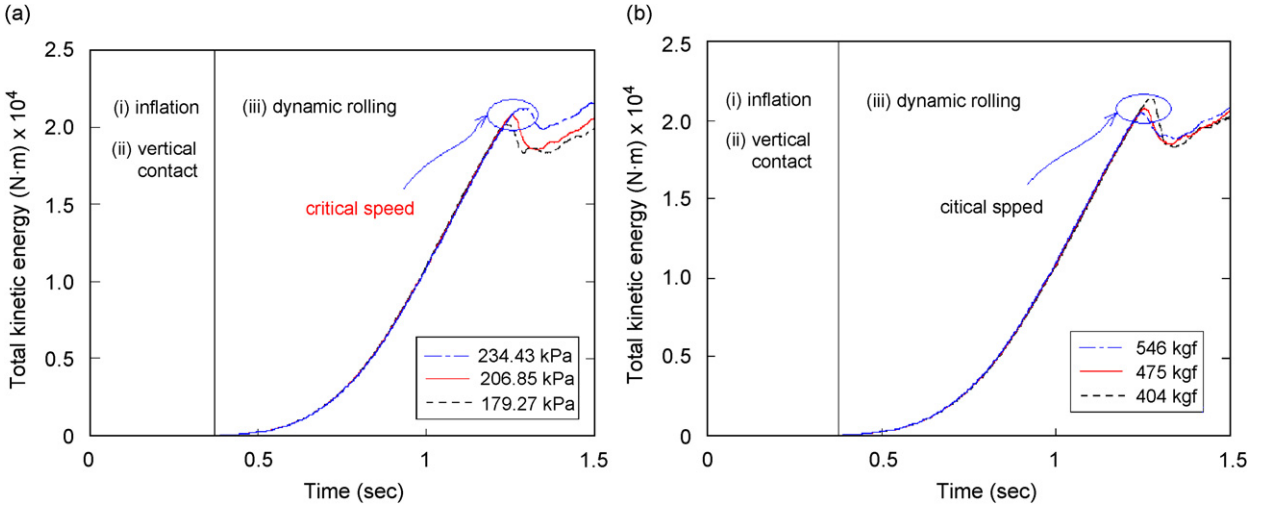

Fig. 11. Variation of the total kinetic energy: (a) to the inflation pressure and (b) to the vertical load.

Table 4
Dependence on both the inflation pressure and the vertical load

Vertical load F_y (kgf)	Critical speed V_c (km/h)		
	Inflation pressure p_i (kPa)		
	179.27	206.85	234.43
404	202	205	212
475	193	199	203
546	184	191	195

speed increases with the inflation pressure for three vertical loads but decreases with the vertical load for three inflation pressures. According to the least-square curve fitting of nine discrete critical speeds, we found that the critical speed is expressed as a bi-linear function of two parameters: $V_c = 241.6725 + 0.41373\, p_i - 0.17019\, F_Y + 0.00178\, p_i F_y$.

5. Conclusion

A numerical technique for predicting the critical speed of tires has been introduced in this paper by utilizing the damped transient dynamic rolling analysis of 3-D patterned tire model. The overall stiffness, the total mass and the structural damping of the patterned tire were accurately reflected by fully taking the detailed tread geometry and the complex tire material composition into consideration and by using the damping coefficient determined by an experiment. The critical speed was measured at the time when the lateral deformation produces a standing wave with a wavelength. The verification experiment confirms the reliability of the proposed technique using 3-D patterned tire models such that the maximum relative error of the predicted critical speeds with respect to the experimental results is less than 5%, in contrast to the simple tire models. On the other hand, the parametric experiments show that the critical speed increases in proportional to the square of the tire inflation pressure, but decreases with the vertical load of the same logarithmic slope.

Acknowledgment

The financial support for this work by the Ministry of Education in Korea under the BK21 program is gratefully acknowledged.

References

[1] S.K. Clark, *Mechanics of Pneumatic Tires*, US Government Printing Office, Washington, DC, 1981.
[2] K. Togo, Standing wave on pneumatic tire at high speed, *Memoirs of the Defense Academy* 4 (1) (1964) 43–56.
[3] F. Ames, Waves in tires, *Textile Research Journal* 20 (1970) 498–503.
[4] A. Chatterjee, J.P. Cusumano, J.D. Zolock, On contact-induced standing waves in rotating tires: experimental and theory, *Journal of Sound and Vibration* 227 (5) (1999) 1049–1081.
[5] Y.D. Kwon, D.C. Prevorsek, Formation of standing waves in radial tires, *Tire Science and Technology, TSTCA* 12 (1–4) (1984) 44–63.
[6] G.R. Potts, C.A. Bell, L.T. Charek, T.K. Roy, Tire vibrations, *Tire Science and Technology, TSTCA* 5 (1977) 202–225.
[7] J. Medzorian, Prediction of aircraft tire critical speed by natural frequency extraction, Internal Report, Wright Laboratories/FIVMA, US Air Force, 1991.
[8] D.M. Turner, Wave phenomenon in tyres at high speed, *Proceedings of Third Rubber Technology Conference*, London, 1954.
[9] W.B. Bickford, E.S. Reddy, On the in-plane vibrations of rotating rings, *Journal of Sound and Vibration* 101 (1985) 13–22.
[10] S.C. Huang, The vibration of rolling tyres in ground contact, *International Journal of Vehicle Design* 13 (1992) 78–95.
[11] E. Vinesse, H. Nicollet, Surface waves on the rotating tyre: an application of fundamental analysis, *Journal of Sound and Vibration* 126 (1988) 85–96.
[12] J. Padovan, On standing waves in tires, *Tire Science and Technology, TSTCA* 5 (2) (1977) 83–101.
[13] W. Soedel, On the dynamic response of rolling tires according to thin shell approximation, *Journal of Sound and Vibration* 41 (1975) 233–246.
[14] R.A. Brockman, J.H. Champion, J.P. Medzorian, Finite element analysis of tire critical speeds, *Computers and Structures* 43 (3) (1992) 581–593.
[15] R.A. Brockman, W.R. Braisted, Critical speed estimation for aircraft tires, *Tire Science and Technology, TSTCA* 22 (2) (1994) 121–144.
[16] D. Zheng, Viscoelastic rolling for tire standing wave simulation, *Proceedings of the Sixth World Congress on Computational Mechanics (WCCM VI)*, Beijing, China, 2004.
[17] J.R. Cho, K.W. Kim, D.H. Jeon, W.S. Yoo, Transient dynamic response analysis of 3-D patterned tire rolling over cleat, *European Journal of Mechanics A/Solids* 24 (2005) 519–531.
[18] J.R. Cho, J.H. Choi, W.S. Yoo, G.J. Kim, J.S. Woo, Estimation of dry road braking distance considering frictional energy of patterned tires, *Finite Elements in Analysis and Design* 42 (2006) 1248–1257.
[19] M. Shiraishi, H. Yoshinaga, A. Miyori, E. Takahashi, Simulation of dynamically rolling tire, *Tire Science and Technology, TSTCA* 28 (2000) 264–276.
[20] J.R. Cho, K.W. Kim, W.S. Yoo, S.I. Hong, Mesh generation considering detailed tread blocks for reliable 3-D tire analysis, *Journal of Advances in Engineering Software* 35 (2004) 105–113.
[21] J.R. Cho, D.Y. Ha, Averaging and finite-element discretization approaches in the numerical analysis of functionally graded materials, *Materials Science and Engineering A* 302 (2) (2001) 187–196.
[22] I.M. Daniel, O. Ishai, *Engineering Mechanics of Composite Materials*, Oxford University Press, New York, 1994.

[23] Hibbitt, Karlsson & Sorensen, Inc., *ABAQUS/Explicit User's Manual*, Ver. 6.3, Pawtucket, 2002.
[24] A.K. Chopra, *Dynamics of Structures: Theory and Applications to Earhtquake Engineering*, Prentice-Hall, New Jersey, 1995.
[25] T. Belytschko, W.K. Liu, B. Moran, *Nonlinear Finite Elements for Continua and Structures*, Wiley, 2000.
[26] J.R. Cho, H.S. Jeong, W.S. Yoo, Multi-objective optimization of tire carcass contours using a systematic aspiration-adjustment procedure, *Computational Mechanics* 29 (2002) 498–509.